energies

MDPI

Article

Grid-Forming Energy Storage Optimization and Adaptive Voltage Control for Rural Networks with High-Penetration Photovoltaic

Tongzhang Wang [1], Ye Tian [2], Hui Li [3], Shang Chen [3] and Haoran Chen [1,*]

[1] College of Information and Electrical Engineering, Shenyang Agricultural University, Shenyang 110866, China; 2023190058@stu.syau.edu.cn
[2] Electric Power Research Institute of State Grid Liaoning Electric Power Co., Ltd., Shenyang 110006, China; tianyemailbox@126.com
[3] China Electric Power Research Institute Wuhan Branch, Wuhan 430074, China; lihui00312@163.com (H.L.); epri_shangchen@163.com (S.C.)
* Correspondence: chenhaoran@syau.edu.cn

Abstract

To address the voltage over-limit issue in rural distribution networks caused by high-penetration distributed photovoltaic (DPV) integration, as well as the frequent voltage disturbances resulting from frequent load switching and variable operating conditions in agricultural grid systems, this paper proposes a dual-layer optimized configuration and adaptive voltage control method for grid-forming energy storage systems. First, an outer-layer siting and sizing model is established with constraints including voltage stability, deviation, network losses, and economic factors. The configuration scheme is solved using the Multi-Objective Particle Swarm Optimization (MOPSO) algorithm. Then, an inner-layer rolling optimized dispatch model is constructed with Model Predictive Control (MPC) as the core, and an adaptive reactive power–voltage control method based on Virtual Synchronous Generator (VSG) control is proposed to enhance transient voltage support under disturbance conditions. Simulation analysis based on an actual 10 kV rural distribution line verifies that the proposed method can effectively mitigate overvoltage issues and alleviate reverse power flow during typical daily operation, while significantly improving node voltage recovery speed and reactive power support capability under voltage disturbances.

Keywords: grid-forming energy storage; siting and sizing; VSG control; dual-layer optimized configuration

Check for updates

Academic Editor: François Vallée

Received: 19 February 2026
Revised: 7 April 2026
Accepted: 28 April 2026
Published: 6 May 2026

Copyright: © 2026 by the authors. Licensee MDPI, Basel, Switzerland. This article is an open access article distributed under the terms and conditions of the Creative Commons Attribution (CC BY) license.

1. Introduction

Under the backdrop of the "Dual Carbon" goals and the rapid development of new energy sources, the integration of distributed photovoltaic (DPV) systems has become a significant feature of distribution networks. As the proportion of DPV output increases, the voltage operation of distribution networks is shifting from a load-dominated pattern characterized by voltage drop at the line end to a bidirectional variation characteristic influenced by the time-varying output of distributed generation. During peak PV output periods, reverse power flow and node voltage rise are prone to occur, while during peak load or periods of rapid irradiance change, voltage sag and disturbances are common [1]. Voltage deviations beyond the permissible range can trigger inverter protection actions

and grid disconnection, affect relay protection coordination, and increase distribution network operation risks. Consequently, voltage compliance under high-penetration DPV conditions has become a critical constraint for distribution network operation [2]. For rural networks with high DPV penetration, overvoltage issues often concentrate at feeder ends, grid connection points, and during periods of high PV output or rapid fluctuation. Due to factors such as limited voltage regulation and energy storage resources in rural grids, single measures struggle to balance compliance, economy, and reliable operation in the long term. Therefore, addressing voltage limit violations requires a coordinated solution spanning planning, operation, and control [3,4].

Extensive research has been conducted on overvoltage mitigation in distribution networks. Studies indicate that energy storage systems (ESSs), as key regulation resources, can provide power compensation through demand-based charging and discharging, thereby reducing network losses and suppressing voltage fluctuations. The rational configuration of grid-forming energy storage in distribution networks is an effective means to address voltage limit violations caused by renewable energy integration [5–7]. However, constrained by factors such as high configuration costs, the optimized configuration of grid-forming energy storage has become a crucial research direction for mitigating voltage limit violations in distribution networks. Reference [8] conducts a quantitative assessment of static voltage stability but lacks a specific analysis on energy storage configuration. Reference [9] proposes a multi-objective optimization model for distribution network systems incorporating battery storage and distributed PV sources. Reference [10] establishes an optimized energy storage capacity configuration model based on typical daily scenarios. Regarding the optimized configuration of grid-forming energy storage, existing research has not considered the optimized management of the state of charge (SOC). For rural networks with frequent load switching and susceptibility to voltage disturbances, optimization results may deviate from the long-term economic viability of equipment operation.

Moreover, due to the intermittency and fluctuation of DPV output, together with the more frequent load switching in rural distribution networks, voltage disturbances are more likely to occur during actual operation [11]. This indicates that, in order to comprehensively address both voltage limit violations and the demand for dynamic voltage regulation under disturbance conditions, it is also necessary to further investigate fast-response control strategies for grid-forming energy storage from the control perspective, so as to enhance its voltage support capability under transient operating conditions. Among the control methods for grid-forming energy storage, Virtual Synchronous Generator (VSG) control emulates the rotational inertia, damping characteristics, and external characteristics of synchronous generators, thereby enabling static inverters to exhibit synchronous-machine-like dynamic response as well as frequency and voltage support capability [12,13], and has become a common control strategy for grid-forming energy storage to participate in voltage regulation and transient support control in distribution networks. Current research on the active support functions of VSG primarily focuses on frequency support, inertia support, related mechanisms, and improvements in control strategies. Reference [14] proposes a VSG control strategy based on fuzzy rules and weight-adaptive MPC, which can reduce frequency deviation and improve system frequency stability. Reference [15] introduces an adaptive control with angular frequency negative feedback, enhancing the transient stability of the system. Reference [16] introduces a distributed secondary reactive power–voltage control structure to achieve average voltage restoration and reactive power sharing proportional to capacity. Reference [17] proposes a coordinated voltage and reactive power control system involving grid-forming energy storage and VSG to improve voltage stability and reactive power regulation capability. Reference [18] achieves stable grid-connected voltage control by modifying the voltage control loop to regulate reactive power and

adjust the output voltage in real time. Regarding the active voltage support provided by grid-forming energy storage, control strategies that consider improving the VSG's voltage support capability under disturbance conditions from the perspective of control parameters are rarely studied.

Based on the above analysis, this study addresses the overvoltage problem in rural networks caused by high-penetration DPV by constructing a dual-layer optimized configuration model for grid-forming energy storage systems. The outer-layer model optimizes the location and capacity of the grid-forming energy storage with the objectives of system voltage stability and operational cost reduction. Building upon the outer-layer model, the inner-layer model optimizes the charging and discharging process of the grid-forming energy storage with the goal of managing its SOC. To address transient voltage fluctuations under disturbances, this study introduces an adaptive mechanism within the VSG control framework. Finally, simulation verification of the designed model is conducted based on a simulation model of a rural network line.

2. Dual-Layer Optimization Configuration Model for Grid-Forming Energy Storage Systems

2.1. Outer Layer Position Capacity Optimization Model

The outer-layer model employs the rated power and capacity of the energy storage system as variables, utilizing a Multi-Objective Particle Swarm Optimization algorithm to optimize the siting and capacity of energy storage devices. Its objectives include maintaining system voltage stability, reducing grid losses, and lowering system operating costs. The constructed multi-objective function is detailed as follows:

(1) Static Voltage Stability Objective Function

Static voltage stability assessment in distribution networks can generally be classified into two categories: branch power-flow-based indices and node voltage limit or margin-based indices. Compared with transmission systems, distribution networks typically consist of a root node, main feeder, lateral branches, and terminal branches, and exhibit significantly different electrical characteristics, including lower voltage levels, shorter line lengths, larger resistance-to-reactance ratios, and relatively higher active power losses. Owing to these characteristics, the voltage stability behavior of distribution networks is more directly governed by branch power transfer capability and receiving-end voltage variation [19,20]. Therefore, based on the impedance characteristics and branch power–flow relationships of distribution feeders, a mathematical model of the branch voltage stability index is established. This model quantifies the static voltage profile after the integration of distributed generation, providing data support for improving weak points in the network voltage [8,21]. The optimization objective is to minimize the static voltage stability index of the weakest branch, thereby enhancing the system's static voltage stability margin:

The circuit is modeled using a π-equivalent circuit. Let the series impedance of branch i-j be $R_{ij} + jX_{ij}$, and let the branch shunt admittance be $G_{ij} + jB_{ij}$. Under steady-state sinusoidal conditions, the receiving-end complex power is expressed as:

$$P_j + jQ_j = \dot{U}_j \left(\dot{I}_{ij} \right)^* \tag{1}$$

where $\dot{U}_j$ is the receiving-end voltage phasor and $\dot{I}_{ij}$ is the series branch current phasor.

Accordingly, the series branch current can be written as:

$$\dot{I}_{ij} = \frac{P_j - jQ_j}{\dot{U}_j^*} + \frac{G_{ij} + jB_{ij}}{2} \dot{U}_j \tag{2}$$

According to the branch voltage equation, the voltage relationship of branch *i-j* is given by:

$$\dot{U}_i - \dot{U}_j = (R_{ij} + jX_{ij})\dot{I}_{ij} \tag{3}$$

Substituting (2) into (3) yields:

$$\dot{U}_i = \left(1 + \frac{(R_{ij} + jX_{ij})(G_{ij} + jB_{ij})}{2}\right)\dot{U}_j + (R_{ij} + jX_{ij})\frac{P_j - jQ_j}{\dot{U}_j^*} \tag{4}$$

Introduce auxiliary variables:

$$\alpha_{ij} = 1 + \frac{(R_{ij} + jX_{ij})(G_{ij} + jB_{ij})}{2} \tag{5}$$

$$\beta_{ij} = (R_{ij} + jX_{ij})(P_j - jQ_j) \tag{6}$$

Multiplying both sides of (4) by $\dot{U}_j^*$ and taking the modulus squared gives:

$$|\alpha_{ij}|^2\left|\dot{U}_j\right|^4 + \left[2\mathrm{Re}\left(\alpha_{ij}^*\beta_{ij}\right) - \left|\dot{U}_i\right|^2\right]\left|\dot{U}_j\right|^2 + |\beta_{ij}|^2 = 0 \tag{7}$$

For the receiving-end voltage to admit a real-valued solution, the discriminant of (7) must satisfy:

$$\Delta_{ij} = \left[\left|\dot{U}_i\right|^2 - 2\mathrm{Re}\left(\alpha_{ij}^*\beta_{ij}\right)\right]^2 - 4|\alpha_{ij}|^2|\beta_{ij}|^2 \geq 0 \tag{8}$$

where Δ_{ij} denotes the discriminant of the quadratic equation associated with $\left|\dot{U}_j\right|^2$. As Δ_{ij} approaches zero, the receiving-end node gradually approaches the static voltage stability limit.

Power distribution networks are typically characterized by short line lengths, a relatively high resistance-to-reactance ratio, and a weak shunt capacitive effect. Under these conditions, the contribution of branch shunt admittance is small, and it can be assumed that:

$$\left|(R_{ij} + jX_{ij})(G_{ij} + jB_{ij})\right| \ll 1 \tag{9}$$

Accordingly, the shunt admittance term in (4) can be neglected, and the branch voltage equation is simplified to:

$$\dot{U}_i = \dot{U}_j + (R_{ij} + jX_{ij})\frac{P_j - jQ_j}{\dot{U}_j^*} \tag{10}$$

Multiplying both sides of (10) by $\dot{U}_j^*$ and taking the modulus squared yields:

$$\left|\dot{U}_j\right|^4 + \left[2(R_{ij}P_j + X_{ij}Q_j) - \left|\dot{U}_i\right|^2\right]\left|\dot{U}_j\right|^2 + \left(R_{ij}^2 + X_{ij}^2\right)\left(P_j^2 + Q_j^2\right) = 0 \tag{11}$$

For it to admit a real-valued solution, its discriminant must satisfy:

$$\left[\left|\dot{U}_i\right|^2 - 2(R_{ij}P_j + X_{ij}Q_j)\right]^2 - 4\left(R_{ij}^2 + X_{ij}^2\right)\left(P_j^2 + Q_j^2\right) \geq 0 \tag{12}$$

Therefore, the simplified branch static voltage stability index is defined as:

$$f_1 = VIS_{ij} = \frac{4\left(R_{ij}P_j + X_{ij}Q_j\right)\left|\dot{U}_i\right|^2 + 4\left(X_{ij}P_j - R_{ij}Q_j\right)^2}{\left|\dot{U}_i\right|^4} \tag{13}$$

where $\dot{U}_i$ and $\dot{U}_j$ are the voltage phasors at nodes i and j, respectively; $\dot{I}_{ij}$ is the series current phasor of branch i-j; P_j and Q_j are the receiving-end active and reactive power of branch i-j, respectively; α_{ij} is the shunt-admittance correction factor; β_{ij} is the impedance–power coupling term.

To evaluate the effect of neglecting branch shunt admittance on the static voltage stability index, a case study analysis is carried out, and the detailed results are provided in Appendix A. The results show that the error between the simplified model and the complete π-equivalent model is very small, and the weak-branch ranking remains unchanged. To further examine how different impedance characteristics affect the accuracy of the voltage stability model, a parametric analysis is performed by varying branch impedance magnitude and R/X ratio. The results indicate that the approximation error increases mainly with impedance magnitude, whereas the influence of R/X variation is limited. These findings confirm the feasibility of neglecting branch shunt admittance in the present study. Accordingly, Equation (13) is adopted as the static voltage stability objective in the subsequent optimization model.

When $VIS_{ij} \leq 1$, it indicates that the static voltage stability of the corresponding node in the distribution network is maintained. The smaller the value of VIS_{ij}, the higher the static voltage stability. When VIS_{ij} = 1, node j is in a voltage critical stability state. The static voltage stability index can be used to analyze and evaluate the voltage distribution in the distribution network in detail. The closer the value of VIS_{ij} is to 1, the more susceptible the node is to triggering voltage collapse.

(2) Node Voltage Deviation Objective Function

Reducing the node voltage deviation in the distribution network system can increase the safety margin against voltage excursions. The optimization objective is formulated to minimize the deviation degree of each node voltage relative to its rated value:

$$f_2 = \sum_{m=1}^{N} |U_m - U_{rated}| \tag{14}$$

$$U_m = U_0 - \sum_{K=1}^{m} \frac{\left(\sum_{m=K}^{N}(P_n - P_{ESS,n}) - P_v\right) r l_K}{U_{K-1}} \tag{15}$$

where U_m is the actual voltage at node m; N is the total number of nodes participating in the statistics; U_0 is the voltage at the head of the line; P_n is the load active power at the n-th node; $P_{ESS,n}$ is the active power output of the grid-forming energy storage at the n-th node; P_v represents the active power injected into the line by distributed photovoltaics.

(3) System Network Loss Objective Function

The optimization objective is to minimize the distribution network operating active power losses:

$$f_3 = \sum_{i,j\in\Omega} X_i \frac{\left(P_{ij}^*\right)^2 + \left(Q_{ij}^*\right)^2}{U_i^2} R_{ij} \tag{16}$$

$$P_{ij}^{*} = P_{ij} - P_{ESS} \tag{17}$$

$$Q_{ij}^{*} = Q_{ij} - Q_{ESS} \tag{18}$$

where P_{ij}^{*} is the equivalent active component on branch (i, j) after considering the effect of energy storage; Q_{ij}^{*} is the equivalent reactive component on branch (i, j) after considering the effect of energy storage.

(4) Voltage Over-Limit Penalty Function

To reduce the risk of system voltage limit violations and improve voltage quality, the optimization objective is to minimize the risk of node voltage exceeding permissible limits [8]:

$$f_4 = \sum_{j \in \Omega}^{n} \rho_j \left(\frac{\Delta V_j}{V_{j,\max} - V_{j,\min}} \right)^2 \tag{19}$$

$$\rho_j = \frac{\deg(j)}{\max_k \deg(k)} \times \frac{\left| V_j - V_{ref} \right|}{V_{ref}} \tag{20}$$

where $\frac{\deg(j)}{\max_k \deg(k)}$ represents the topological importance of the node, $\deg(j)$ is the number of direct branch connections at node j; $\max_k \deg(k)$ is the maximum number of connections among all nodes in the network; V_j is the actual voltage at node j; $V_{j,\min}$ and $V_{j,\max}$ are the lower and upper voltage limits of node j respectively.

(5) Grid-Forming Energy Storage Economic Objective Function

The economic objective function of grid-forming energy storage primarily includes reducing line-loss costs, increasing the revenue from enhanced renewable energy utilization by curtailing energy waste, and covering the construction and investment costs of the grid-forming energy storage system.

$$f_5 = \sum_{t=1}^{T} \sum_{i=1}^{38} C_{loss} L_{i,t} + \sum_{t}^{T} \sum_{i}^{38} C_{curt} E_{i,t} + C_a \tag{21}$$

where C_{loss} denotes the cost per unit of line loss; $L_{i,t}$ represents the line loss at node i at time t; C_{curt} indicates the cost per unit of curtailed energy; $E_{i,t}$ is the curtailed PV energy at time t; C_a refers to the annualized investment cost of the grid-forming energy storage system.

$$C_a = C_{in} CRF(r, n) \tag{22}$$

where C_{in} represents the initial investment cost of the energy storage equipment; $CRF(r, n)$ denotes the capital recovery factor, which converts the one-time investment cost into an annualized equivalent expense.

$$C_{in} = C_e \times E_b + C_p \times P_b \tag{23}$$

where C_e and C_p represent the unit cost of rated capacity and the unit cost of rated power for the grid-forming energy storage, respectively; E_b denotes the rated capacity of the grid-forming energy storage system; P_b denotes the rated power of the grid-forming energy storage system.

$$CRF(r, n) = \frac{r(1+r)^n}{(1+r)^n - 1} \tag{24}$$

where r is the annual interest rate, and n is the service life in years.

Considering that the optimization of grid-forming energy storage systems involves multiple heterogeneous objectives such as voltage stability indices, voltage deviation, net-

work losses, and economic efficiency, there are significant differences among the indicators in terms of dimension, numerical range, and physical meaning. Direct multi-objective weighting would cause certain indicators to dominate numerically, thereby affecting the rationality of the optimization results. To address this issue, an improved Min–Max normalization method is adopted to perform dimensionless processing of each objective indicator. For any given indicator, its normalized value is defined as:

$$f(x) = \frac{x - \min(x)}{\max(\max(x) - \min(x), \varepsilon)} \tag{25}$$

where x represents the original data vector to be normalized; $\max(x) - \min(x)$ denotes the range or variation span of the vector, reflecting the degree of differentiation of the indicator among all nodes; ε is the machine-precision constant, a small positive constant introduced to avoid division by zero when $\max(X) = \min(X)$. After normalization, all node-level indicators are mapped into the interval $[0, 1]$, and a larger normalized value indicates that the node is weaker with respect to the corresponding indicator.

Based on the normalized indicators, the basic comprehensive weakness score of node i is defined as:

$$S_i = \omega_1 f_1 + \omega_2 f_2 + \omega_3 f_3 + \omega_4 f_4 + \omega_5 f_5 \tag{26}$$

where ω_1, ω_2, ω_3, ω_4, and ω_5 are weighting coefficients that sum to 1.

After normalization, the relative influence of each indicator on the comprehensive score is explicitly determined by the preset weights rather than by the original numerical magnitude of the raw indicator.

The normalized outer-layer multi-objective function is given as:

$$\min F_1 = \min S_i \tag{27}$$

2.2. Inner-Layer Dynamic Optimized Control Model

In the operation of rural distribution networks, the SOC management of grid-forming energy storage systems determines the sustainability of their voltage support capability. Distributed photovoltaic output in rural distribution networks is intermittent and fluctuating, load switching is frequent, and voltage disturbances are prone to occur. Grid-forming energy storage must frequently charge and discharge to mitigate power fluctuations, resulting in substantial variations in SOC. Excessive SOC fluctuations increase the number of charge–discharge cycles, accelerate the aging of the energy storage system, and weaken operational safety and the duration of available support. Therefore, based on the siting and sizing results obtained from the outer-layer model, the inner-layer dynamic optimized control model is established with MPC as the core to optimize the charging and discharging process of the grid-forming energy storage system.

2.2.1. MPC Principle and Prediction Model

MPC predicts the future behavior of the controlled system over a finite horizon based on the current measured state and forecast information, determines the optimal future control sequence by solving a constrained optimization problem, and applies only the first control action at each sampling instant. At the next sampling instant, the measured states are updated and the optimization is repeated in a receding-horizon manner. This rolling optimization mechanism is particularly suitable for grid-forming energy storage systems with time-varying operating conditions and multiple practical constraints.

To implement the aforementioned rolling optimization scheduling strategy, it is necessary to establish a discrete-time predictive model for the inner-loop MPC. Given that both overvoltage and reverse power flow issues in the feeder are closely related to changes in

the feeder's net load, the predicted net load of the feeder is used as the fundamental input for the inner-loop optimization model. Combined with the energy storage charging and discharging power and the SOC state equation, this describes the dynamic evolution of the energy storage active power and SOC, providing a model foundation for subsequent objective function formulation and rolling optimization solutions. Accordingly, the predicted feeder net demand at time step K is defined as:

$$d(K) = \hat{P}_L^{\Sigma}(K) - \hat{P}_{PV}^{\Sigma}(K) \tag{28}$$

where $\hat{P}_L^{\Sigma}(K)$ and $\hat{P}_{PV}^{\Sigma}(K)$ are the forecasted total load power and total photovoltaic power of the feeder, respectively.

Define $P_i^{es}(K)$ as the active power of the i-th grid-connected energy storage unit at time K. The active power exchange between the feeder and the upstream grid can be expressed as:

$$P_g(K) = d(K) - \sum_{i \in \Omega_{ES}} P_i^{es}(K) \tag{29}$$

where Ω_{ES} denotes the set of energy storage units determined by the outer-layer site selection and capacity allocation model; $P_i^{es}(K) > 0$ indicates discharge, and $P_i^{es}(K) < 0$ indicates charging.

To suppress abrupt feeder power fluctuation and alleviate reverse power flow during high-photovoltaic-output periods, the feeder power reference is generated by low-pass filtering the predicted net demand:

$$P_g^{ref}(K) = \max\left\{0, \beta P_g^{ref}(K-1) + (1-\beta)d(K)\right\} \tag{30}$$

where β is the smoothing factor, $0 < \beta < 1$.

For the i-th storage unit, the control increment is defined as:

$$\Delta P_i^{es}(K) = P_i^{es}(K) - P_i^{es}(K-1) \tag{31}$$

The power update equation is:

$$P_i^{es}(K+1) = P_i^{es}(K) + \Delta P_i^{es}(K) \tag{32}$$

The SOC state update equation is written as:

$$SOC_i(K+1) = SOC_i(K) - \alpha_i(k) P_i^{es}(K+1) \tag{33}$$

$$\alpha_i(k) = \begin{cases} \frac{\Delta t}{\eta_i^{dis} E_i}, P_i^{es}(K) \geq 0 \\ \frac{\eta_i^{ch} \Delta t}{E_i}, P_i^{es}(K) < 0 \end{cases} \tag{34}$$

where E_i is the rated energy capacity of the i-th storage unit, and η_i^{ch} and η_i^{dis} are the charging and discharging efficiencies, respectively.

Accordingly, the state vector, control vector, and output vector are defined as:

$$x(K) = [P_1^{es}(K) \cdots P_M^{es}(K) SOC_1(K) \cdots SOC_M(K)]^T \tag{35}$$

$$u(K) = [\Delta P_1^{es}(K) \cdots \Delta P_M^{es}(K)]^T \tag{36}$$

$$y(K) = \left[P_g^{es}(K) SOC_1(K) \cdots SOC_M(K)\right]^T \tag{37}$$

The inner-layer model is then written in discrete state-space form as:

$$x(K+1) = A(K)x(K) + B(K)u(K) \tag{38}$$

$$y(K) = Cx(K) + Dd(K) \tag{39}$$

$$A(K) = \begin{bmatrix} I_M & 0 \\ -\Gamma(K) & I_M \end{bmatrix} \tag{40}$$

$$B(K) = \begin{bmatrix} I_M \\ -\Gamma(K) \end{bmatrix} \tag{41}$$

$$\Gamma(K) = \begin{bmatrix} \alpha_1(K) & 0 & \cdots & 0 \\ 0 & \alpha_2(K) & \cdots & 0 \\ \vdots & \vdots & \ddots & \vdots \\ 0 & 0 & \cdots & \alpha_M(K) \end{bmatrix} \tag{42}$$

$$C = \begin{bmatrix} -1_{1\times M} & 0_{1\times M} \\ 0_{M\times M} & I_M \end{bmatrix} \tag{43}$$

$$D = \begin{bmatrix} 1 \\ 0_{M\times 1} \end{bmatrix} \tag{44}$$

where I_M is the M-dimensional identity matrix and $1_{1\times M}$ is a row vector of ones.

2.2.2. MPC Optimization Objective Functions

Based on the inner-layer MPC prediction model, the optimization objectives are to suppress feed power fluctuations, reduce SOC fluctuations, and limit excessive total charge–discharge depth:

$$\min F_2 = \min(f_6 + f_7 + f_8) \tag{45}$$

(1) Power Fluctuation Mitigation Objective Function

Sharp fluctuations in the output of energy storage can affect system stability. By suppressing the magnitude of output variations between adjacent time intervals, it helps mitigate the power imbalance between generation and load. Therefore, the optimization objective is to minimize the output fluctuation level of the energy storage over time.

$$f_6 = \sum_{t=1}^{T-1} \left| P_{grid}(t+1) - P_{grid}(t) \right|^2 \tag{46}$$

where $P_{grid}(t)$ represents the output power of the grid-forming energy storage at time t.

(2) SOC Fluctuation Minimization Objective Function

Frequent and large fluctuations in the SOC can weaken the sustained regulation capability of the energy storage system and accelerate its performance degradation. Maintaining a relatively stable SOC helps improve the operational reliability of the energy storage. Therefore, the optimization objective is to minimize the deviation of the energy storage SOC over the dispatch period.

$$f_7 = \sum_{t=1}^{T-1} \left| SOC_m(t+1) - SOC_m(t) \right|^2 \tag{47}$$

where $SOC_m(t)$ represents the state of charge of the grid-forming energy storage at node m at time t.

(3) Minimization of Total Charge–Discharge Depth Objective Function

Excessively deep charge–discharge cycles can significantly accelerate battery aging and shorten service life. Limiting the depth of discharge helps delay the degradation of energy storage performance. Therefore, the optimization objective is to suppress operational conditions where the SOC approaches its upper or lower limits, thereby reducing the overall depth of charge and discharge.

$$f_8 = \sum_{t=1}^{T}\left[\lambda \max(0, SOC_{\min} - SOC_m(t))^2 + \lambda \max(0, SOC_m(t) - SOC_{\max})^2\right] \quad (48)$$

where $SOC_{\max}$ denotes the recommended upper operational SOC boundary; $SOC_{\min}$ denotes the recommended lower operational SOC boundary; λ represents the penalty coefficient, which intensifies as the SOC approaches the boundary.

In the rolling optimization process, the above three objectives are coordinated within the same MPC framework. In addition, the boundary penalty term in f_8 is used to strengthen the protection effect when the SOC approaches its upper or lower operational boundary, thereby coordinating feeder power smoothing and sustainable SOC management.

2.2.3. Receding-Horizon Optimization and Solution Mechanism

At each sampling instant K, the MPC constructs a finite-horizon optimization problem according to the current measured state $x(K)$, the forecast information, and the prescribed reference trajectory. After stacking the future control increments over the control horizon, the decision vector is written as:

$$U(K) = \left[u^T(K \mid K) u^T(K+1 \mid K) \cdots u^T(K+N_c-1 \mid K)\right]^T \quad (49)$$

The MPC problem described above can be reformulated as the following standard quadratic programming problem:

$$\min_{U(K)} \frac{1}{2} u^T(K) H(K) U(K) + f^T(K) U(K) \quad (50)$$

where $H(K)$ is the Hessian matrix and $f(K)$ is the coefficient vector of the linear term.

In each step of the rolling optimization, only the first optimal control input $u^T(K|K)$ is applied to the energy storage unit. At the next sampling time, the system state is updated based on the latest measured values, the prediction time domain is advanced by one step, and the optimization process is repeated. This forms a complete rolling optimization mechanism of "measurement—prediction—optimization—execution—re-prediction," enabling the inner-layer model to continuously adapt to the time-varying characteristics of PV output and load demand.

2.3. Constraints

In the optimization process, to ensure the feasibility of energy storage siting and capacity allocation decisions, the discreteness and engineering rationality of the planning scheme, and the safe dynamic operation of the energy storage system during rolling optimization, the proposed dual-layer optimization model must satisfy the following constraints: the distribution network node power balance constraints; the discrete siting and installation-capacity constraints of grid-forming energy storage; the rated power and rated energy capacity constraints; the corresponding capacity-to-power coupling constraints; the charging/discharging power constraints; the SOC state-update and upper/lower bound constraints; and the ramp-rate constraints of the grid-forming energy storage system.

(1) Node Power Balance Constraints

$$P_{it} = U_{it}\sum_{j=1}^{N} U_{jt}\left[G_{ij}\cos\left(\delta_{it}-\delta_{ji}\right)+B_{ij}\sin\left(\delta_{it}-\delta_{ji}\right)\right] \tag{51}$$

$$Q_{it} = U_{it}\sum_{j=1}^{N} U_{jt}\left[G_{ij}\sin\left(\delta_{it}-\delta_{jt}\right)+B_{ij}\cos\left(\delta_{it}-\delta_{jt}\right)\right] \tag{52}$$

where P_{it} is the injected active power at grid node i at time t; Q_{it} is the injected reactive power at grid node i at time t; U_{it} and U_{jt} are the voltages at nodes i and j at time t, respectively; δ_{it} is the phase angle at node i at time t; δ_{jt} is the phase angle at node j at time t; G_{ij} is the real part (conductance) of the element in the i-th row and j-th column of the nodal admittance matrix; B_{ij} is the imaginary part (susceptance) of the element in the i-th row and j-th column of the nodal admittance matrix; N is the total number of nodes.

(2) Power Constraints for Charging and Discharging of Grid-Connected Energy Storage Batteries

$$P_{c,\max} = \min\{P_{c,rate}[E_{ES}-E_{t-\Delta t}]/(\Delta t\eta_c)\} \tag{53}$$

$$P_{F,\max} = \min\{P_{F,rate}[E_{t-\Delta t}-E_{ES}]\eta_F/\Delta t\} \tag{54}$$

where $P_{c,rate}$ is the rated charging power of the grid-forming energy storage battery; $P_{F,rate}$ is the rated discharging power of the grid-forming energy storage battery; E_{ES} is the capacity of the grid-forming energy storage battery; $E_{t-\Delta t}$ is the stored energy of the grid-forming energy storage battery during the period $t-\Delta t$.

(3) Intrinsic Performance Constraints of Grid-Forming Energy Storage Batteries

$$\begin{cases} S_{oc,\min} \le S_{oc}(t) \le S_{oc,\max} \\ P_{C,\min} \le P_{C,t} \le P_{C,\max} \\ P_{F,\min} \le P_{F,t} \le P_{F,\max} \end{cases} \tag{55}$$

where $S_{oc,\max}$ and $S_{oc,\min}$ are the maximum and minimum state of charge of the grid-forming energy storage system, respectively; $P_{C,\max}$ and $P_{C,\min}$ are the upper and lower limits for the charging power of the grid-forming energy storage battery, respectively; $P_{F,\max}$ and $P_{F,\min}$ are the upper and lower limits for the discharging power of the grid-forming energy storage battery, respectively.

Updating the state of charge of energy storage devices:

$$SOC_i(t+1) = SOC_i(t) + \frac{\eta_c P_{C,i}(t)\Delta t}{E_i} - \frac{P_{F,i}(t)\Delta t}{\eta_F E_i} \tag{56}$$

where η_c and η_F are the charging efficiency and discharging efficiency, respectively; Δt is the dispatch time step; and E_i is the rated energy capacity of the i-th storage unit.

(4) Discrete Siting and Installation-Quantity Constraints

Since the deployment locations of grid-forming energy storage belong to a discrete planning decision, a binary variable y_i is introduced to represent the installation status of candidate nodes:

$$y_i \in \{0,1\},\ i = 1,2,\ldots,N \tag{57}$$

where $y_i = 1$ indicates that a grid-forming energy storage unit is installed at node i, and $y_i = 0$ indicates that no storage unit is installed at that node.

A higher number of installed grid-forming energy storage systems leads to an increased overall cost. Therefore, the following constraint is imposed on the installation quantity of grid-forming energy storage:

$$\sum_{j \in S} y_i \leq K_{\max} \tag{58}$$

where $\sum_{j \in S} y_i$ is the number of selected nodes.

(5) Rated Power and Rated Energy Capacity Constraints

The rated energy capacity and rated power of the grid-forming energy storage units must remain within the permissible range.

$$y_i E_{i,\min} \leq E_i \leq y_i E_{i,\max} \tag{59}$$

$$y_i P_{i,\min} \leq P_i \leq y_i P_{i,\max} \tag{60}$$

where E_i and P_i denote the rated energy capacity and rated power of the grid-forming energy storage installed at node i, respectively.

(6) Capacity–Power Coupling Constraints

The rated power and rated energy capacity of grid-connected energy storage systems should satisfy the actual capacity–power coupling relationship.

$$\alpha E_i \leq P_i \leq \beta E_i \tag{61}$$

where α and β denote the lower and upper bounds of the allowable power-to-energy ratio, respectively.

(7) Rolling Scheduling Slope Rate Constraint

To prevent excessive fluctuations in the charging and discharging power of energy storage systems between adjacent scheduling periods, it is necessary to ensure that the ramp rate of the energy storage system remains within a reasonable range.

$$-\Delta P_i^{\max} \leq P_i(t) - P_i(t-1) \leq \Delta P_i^{\max} \tag{62}$$

where $P_i(t)$ denotes the net active power output of the iii-th grid-forming energy storage unit at time t; $\Delta P_i^{\max}$ represents the maximum allowable power variation between two consecutive dispatch intervals.

2.4. Solving Process for Dual-Layer Models

Multi-Objective Particle Swarm Optimization (MOPSO) is an effective method for solving complex nonlinear multi-objective optimization problems. By simulating swarm intelligence and leveraging information sharing and co-evolution among particles, this method searches for Pareto-optimal solutions in the solution space. In the two-level optimization model for grid-connected energy storage proposed in this paper, the outer layer employs a multi-objective optimization method based on MOPSO, treating the site selection and capacity determination of grid-connected energy storage as decision variables. This process achieves dynamic search of the solution space through iterative updates of particle velocity and position, while utilizing non-dominance ordering and the crowding distance criterion to maintain the compactness of the Pareto solution set, and employing a constraint handling mechanism to ensure the feasibility of the solutions. Specifically, the feasibility screening of candidate solutions is conducted under operating conditions

consistent with the inner-layer MPC, including PV/load time-series curves, SOC upper and lower limits, charge/discharge efficiency, and scheduling time steps, with the outer-layer solution determined based on subsequent operational requirements. Given that the outer-loop optimization problem involves multiple objectives, constraints, and nonlinearities, and that the Pareto front still contains multiple candidate solutions with trade-offs, this study further introduces an information-entropy-weighted TOPSIS method to rank the Pareto-dominant solutions, thereby determining an optimal configuration that balances voltage constraints, economic benefits, and engineering feasibility.

The inner-layer model employs MPC for rolling optimization. Based on the results obtained from the outer layer regarding the site selection and capacity determination of grid-connected energy storage, the inner layer dynamically optimizes the power output of the energy storage system to adapt to the time-varying characteristics of PV output and load fluctuations. In this process, the installation locations, rated power, and rated energy storage capacity determined by the outer layer are input into the inner layer as fixed configuration parameters, while the inner layer performs rolling operational optimization and state updates under the given configuration conditions. Therefore, through the collaborative solution of the inner and outer layer models, the method proposed in this paper not only ensures the rationality of the energy storage configuration scheme at the planning level and its static operational feasibility but also enhances the system's dynamic response capability at the operational level, thereby forming a comprehensive "planning-operation" integrated optimization configuration scheme for grid-forming energy storage. The specific solution process is shown in Figure 1.

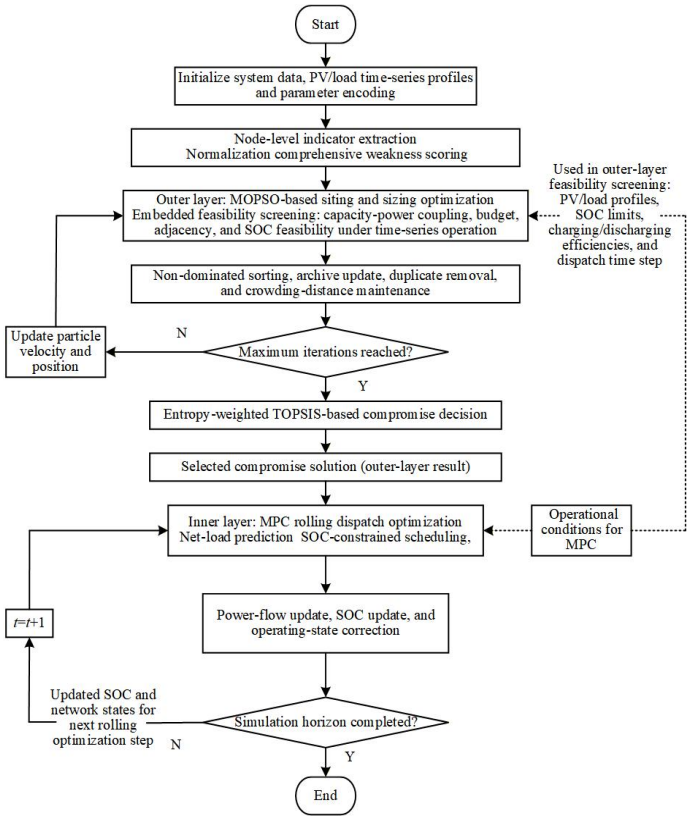


Figure 1. Flowchart for solving the double-layer model.

The detailed solution procedure of the proposed inner/outer dual-layer optimization model is as follows:

Step 1: Based on the time-series power flow simulation results, the voltage of each node, branch power flows, and line parameters of the distribution network are extracted. Considering factors such as node voltage violation risk, network loss contribution, voltage deviation, and topological importance, each node is subjected to dimensionless processing to construct a comprehensive weakness score, providing an a priori basis for the siting of grid-forming energy storage.

Step 2: In the outer-layer model, a multi-objective optimization problem is formulated with the installation location, rated power, and capacity of the grid-forming energy storage as decision variables. The Multi-Objective Particle Swarm Optimization (MOPSO) algorithm is employed to search the solution space, and the diversity of the solution set is maintained through non-dominated sorting and crowding distance, yielding a Pareto optimized solution set that satisfies system voltage quality, stability, and economic requirements.

Step 3: Employ the TOPSIS method weighted by information entropy to further rank the set of Pareto non-dominated solutions obtained from the outer layer and comprehensively evaluate each candidate solution based on its relative proximity to the positive and negative ideal solutions. Select the Pareto solution with the highest overall proximity to the ideal solutions as the optimized compromise, thereby determining the final site locations and capacity configurations for the grid-forming energy storage system.

Step 4: Input the site locations, rated power, and rated energy storage capacity of the grid-forming energy storage system—determined by the outer-loop optimization—into the inner-loop model as known configuration parameters. With MPC as the core, the charging/discharging power of the grid-forming energy storage within a typical day is optimized through rolling optimization, subject to SOC constraints. The optimized output sequence for each time interval is obtained.

Step 5: Based on the active power output results of the grid-forming energy storage derived from the inner-layer optimization, the available reactive power capacity at the corresponding time intervals is calculated, enabling the grid-forming energy storage to participate in voltage regulation while satisfying energy constraints. The system operating status is updated via power flow calculation, and the SOC of the grid-forming energy storage is corrected accordingly.

Step 6: The inner-layer dynamic optimization and state update process is repeatedly executed until the full typical day simulation is completed. Through the coordinated solution of the inner and outer dual-layer models, the proposed approach ensures that the grid-forming energy storage configuration scheme is rational at the planning level and implementable at the operational level.

3. Converter Control Strategy Based on VSG

VSG control introduces the equivalent rotor motion equations and electromagnetic characteristics of synchronous machines into inverter control, enabling grid-forming energy storage converters to possess inertia, damping, and voltage/frequency regulation capabilities, thus providing an effective control means for transient voltage regulation.

As shown in Figure 2, the energy storage battery is connected to the voltage source grid-connected inverter via the DC side. The inverter adopts VSG control to emulate the external characteristics of a synchronous generator, presenting itself as a controlled voltage source with controllable amplitude and phase, thereby possessing frequency and voltage regulation capabilities. VSG control generates the frequency and amplitude references for the inverter output voltage through active power–frequency and reactive power–voltage regulation, respectively, based on the active/reactive power feedback calculated from the grid-connected point voltage and current. Meanwhile, virtual inertia and damping are incorporated to provide inertia and damping support. Additionally, the introduced virtual

impedance emulates impedance characteristics, enhancing the stability of grid-connected operation and voltage support capability. The variables in the Figure are defined as follows: L_f is the filter inductor; C_f is the filter capacitor; Z_g is the equivalent impedance; V_s is the terminal voltage.

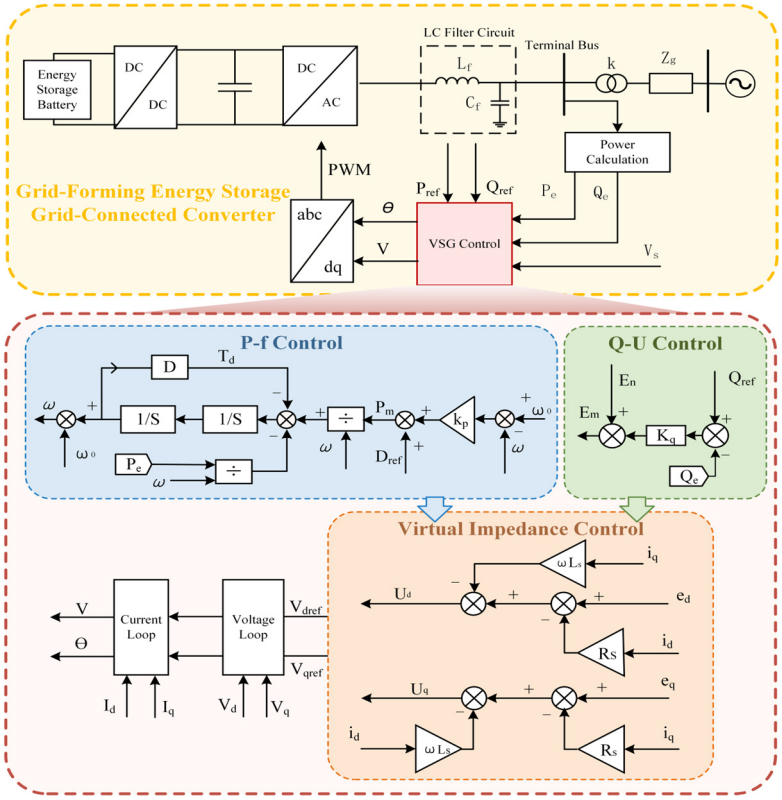


Figure 2. Topology of the VSG-controlled grid-connected converter.

3.1. VSG Control

VSG control enables the converter to provide voltage and frequency regulation capabilities by emulating the external characteristics of synchronous generators, thereby supplying damping and inertia support to the system while allowing flexible adjustability of damping and inertia parameters. The power outer loop is a critical component of VSG control, primarily consisting of active power–frequency control and reactive power–voltage control. Based on the rotor motion equations of synchronous generators and the primary frequency regulation characteristics, the active power–frequency control loop can be established.

$$\begin{cases} J\frac{d\omega}{dt} = \frac{P_m}{\omega_0} - \frac{P_e}{\omega_0} - D(\omega - \omega_0) \\ P_m = P_{ref} + K_p(\omega - \omega_0) \\ \frac{d\delta}{dt} = \omega \end{cases} \tag{63}$$

where J is the virtual moment of inertia of the VSG; D is the damping coefficient representing the damping characteristics of the generator; K_p is the active power–frequency droop coefficient; P_e is the actual active power output of the Virtual Synchronous Generator; P_m is the mechanical power; P_{ref} is the reference value of active power; ω_0 is the rated angular frequency.

By emulating the primary voltage regulation characteristics and excitation regulation mechanism of traditional synchronous generators, the VSG achieves reactive power regulation and voltage control.

$$E_m = K_q\left(Q_{ref} - Q_e\right) + U_n \tag{64}$$

where E_m is the equivalent excitation voltage in VSG control; U_n is the excitation voltage reference under steady-state operation; K_q is the reactive power–voltage droop coefficient; Q_{ref} is the reference value of reactive power; Q_e is the actual reactive power output of the Virtual Synchronous Generator.

The grid-forming converter based on VSG control achieves frequency and voltage regulation through active power–frequency control and reactive power–voltage control. Its external characteristic behaves as a controlled voltage source with series impedance and controllable amplitude and phase [22], as illustrated in Figure 3.

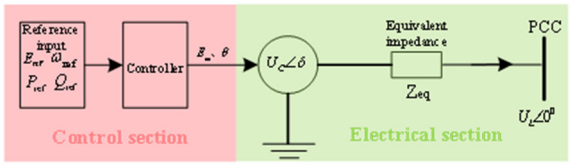


Figure 3. Equivalent external characteristics of the grid-forming converter.

Where Z_{eq} is the series equivalent impedance of the grid-forming converter.

To ensure the correctness of the control quantities and better simulate the quasi-static characteristics of synchronous generators, a virtual impedance loop is added to emulate the stator resistance and synchronous reactance of the synchronous machine.

$$\begin{cases} U_d = e_d - R_s i_d + \omega L_s i_q \\ U_q = e_q - R_s i_q + \omega L_s i_d \end{cases} \tag{65}$$

where U_d and U_q are the voltage reference values set for the d-axis and q-axis components in the voltage–current closed loop, respectively. These are key signals used by the control algorithm to guide current regulation in order to achieve the desired voltage output; e_d and e_q are the virtual voltage components along the d-axis and q-axis, respectively; i_d and i_q are the d-axis and q-axis components of the converter output current; R_s denotes the introduced virtual resistance; L_s denotes the introduced virtual inductance.

3.2. Reactive Power–Voltage Droop Coefficient-Based Adaptive VSG Control Strategy

In the conventional reactive power–voltage droop control of VSG, the commonly used voltage regulation coefficient is defined as the ratio of voltage variation to reactive power variation, as expressed in the following equation:

$$K_q = \frac{\Delta U}{\Delta Q} \tag{66}$$

According to the reactive power–voltage regulation equation of VSG, the voltage regulation coefficient in conventional VSG reactive power–voltage control is typically a fixed value, with the reactive power reference set to $Q_{ref} = 0$. The relationship between the voltage E and reactive power Q under this control mode is illustrated in Figure 4.

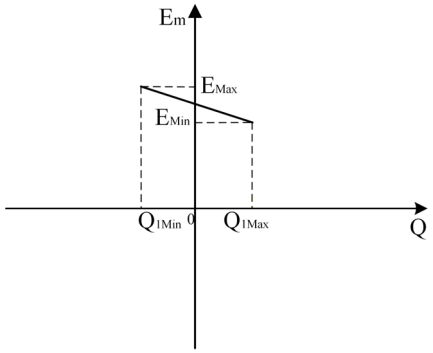


Figure 4. Reactive power–voltage relationship under conventional VSG control.

In Figure 4, $Q_{1\max}$ represents the reactive power output of the energy storage system when the equivalent excitation voltage decreases to its minimum allowable value $E_{\min}$. $Q_{1\min}$ represents the reactive power output of the energy storage system when the equivalent excitation voltage increases to its maximum allowable value $E_{\max}$; this value is negative and corresponds to the maximum reactive power absorbed by the energy storage system.

When the energy storage system operates under different working conditions, its active power output varies in real time to satisfy the system power balance, leading to simultaneous changes in its available reactive power capacity. When the reactive power capacity is sufficient, a smaller droop coefficient is adopted. Within the allowable variation range of the reference potential, the reactive power regulation range expands, enabling the energy storage to provide stronger reactive power support. As illustrated in the figure, conventional VSG control employs a fixed voltage regulation coefficient, making it difficult to adjust the droop characteristics in response to changes in reactive power capacity. Consequently, the reactive power support potential of the grid-connected energy storage system is underutilized, and its voltage support capability is limited.

When operating in grid-connected mode, the grid-forming energy storage system possesses bidirectional power transfer capability. When a power deficit occurs at the grid connection point, the energy storage battery discharges to compensate for the power demand; conversely, when there is a power surplus at the grid connection point, the excess power is used to charge the energy storage battery. Under the premise that the state of charge (SOC) meets the requirements, the reactive power support capability that the grid-forming energy storage can provide under bidirectional charging/discharging operating conditions is jointly constrained by the apparent power and active power, which can be specifically expressed as:

$$\begin{cases} Q_t^{Max} = \sqrt{S_{ESS}^2 - P_t^2} \\ Q_t^{Min} = -\sqrt{S_{ESS}^2 - P_t^2} \end{cases} \tag{67}$$

where Q_t^{Max} and Q_t^{Min} are the upper and lower limits of the reactive power of the grid-forming energy storage at time t; S_{ESS} is the apparent power of the grid-forming energy storage system; P_t is the active power of the grid-forming energy storage system at time t.

The active and reactive power output ranges of the energy storage system during charging and discharging are shown in Figure 5.

As shown in Figure 5, the smaller the active power of the energy storage, the larger the remaining capacity available for reactive power support. Consequently, at that moment, the potential for reactive power support in response to voltage dips at the grid connection point is also stronger.

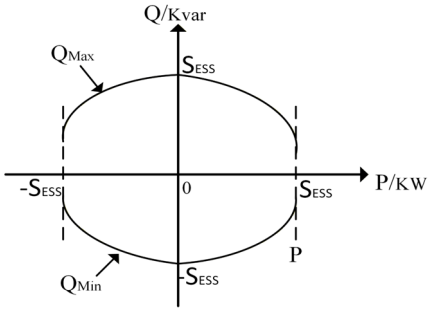


Figure 5. Active and reactive power capacity range for bidirectional energy storage operation.

Under the conventional fixed reactive power–voltage droop control strategy, the reactive power capacity of grid-forming energy storage available for voltage support is often underutilized, resulting in a certain degree of waste. To better release the reactive power support capability of the grid-forming energy storage system under fault conditions, the available reactive power capacity at any given moment is introduced into the adaptive reactive power–voltage proportional coefficient. This enables rapid adjustment of reactive power output according to the operational state of the energy storage, thereby enhancing the transient stability of the grid-forming energy storage system. Integrating the bidirectional operation characteristics of grid-forming energy storage and incorporating the correction of reactive power capacity, the expression for the adaptive reactive power–voltage droop coefficient K_q is as follows:

$$K_{q,t} = \frac{\Delta U_{Max}}{Q_t^{Max} - Q_t^{Min}} \tag{68}$$

where ΔU_{Max} is the maximum allowable voltage fluctuation range at the grid connection point. According to the applicable grid code for 10 kV distribution networks, this value is taken as 0.14 pu.

The adaptive adjustment of the proportional coefficient serves to update the reactive power capacity based on the active power output, taking into account the bidirectional operating characteristics of the energy storage, thereby adaptively correcting the VSG reactive power–voltage regulation coefficient. Accordingly, under different operating conditions, the active power output of the energy storage varies, and the corresponding reactive power–voltage regulation coefficient for each condition is calculated using the proposed formula. The analysis results are presented in Figure 6.

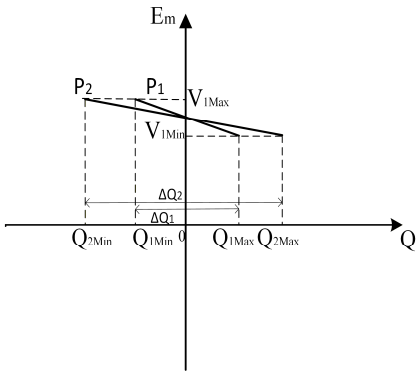


Figure 6. Reactive power capacity of energy storage under different operating conditions.

When the active power of the energy storage system is P_1 and P_2, respectively, with $P_2 < P_1$, the reactive power capacity that the system can provide to the grid differs between these two conditions. Under these two operating conditions, the active power output P_2 corresponds to a smaller reactive power–voltage droop coefficient K_q and a larger reactive

power regulation range. In contrast, the active power output P_1 corresponds to a larger reactive power–voltage droop coefficient K_q and a smaller reactive power regulation range.

The grid-connected structure of the grid-forming energy storage system with the improved adaptive reactive power–voltage droop coefficient is shown in Figure 7.

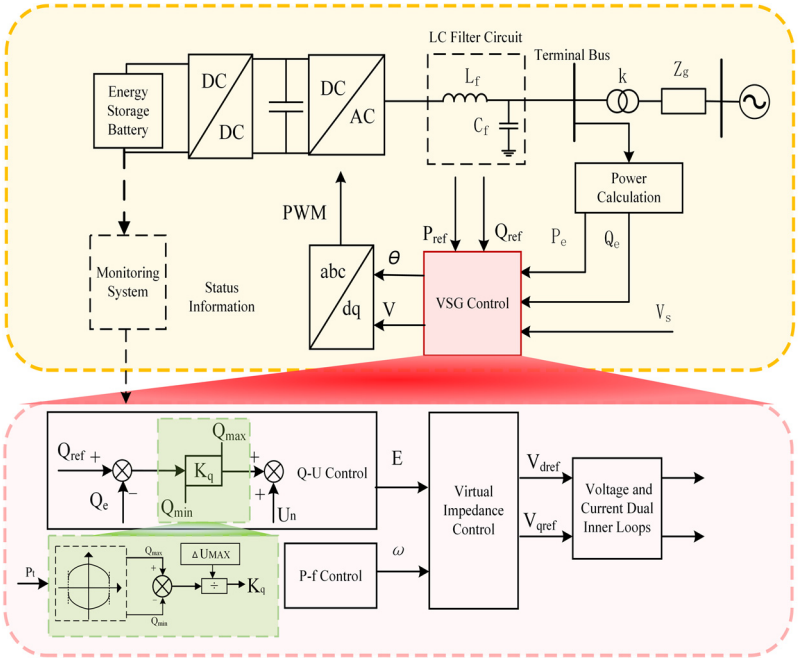


Figure 7. Topology of the improved grid-connected converter.

According to Figure 7, the proposed improvement preserves the basic VSG control structure while introducing, in the Q–U control loop, an adaptive regulation coefficient K_q that is updated according to the operating state of the energy storage system. Specifically, the controller first calculates the reactive power capacity limits $Q_{\max}$ and $Q_{\min}$ under the current operating condition based on the instantaneous active power output P_t of the energy storage system and then determines the adaptive coefficient K_q online in combination with the maximum allowable voltage deviation $\Delta U_{\max}$. The obtained coefficient is subsequently incorporated into the Q–U control loop of the VSG to adaptively adjust the regulation strength associated with the reactive power term, thereby modifying the adjustment amplitude of the equivalent excitation voltage E. After passing through the virtual impedance loop and the dual voltage–current inner loops, the inverter output voltage and reactive current are correspondingly regulated, enabling adaptive adjustment of reactive power support capability under different active power operating conditions. Compared with the fixed-coefficient control strategy, the proposed method allows the voltage support strength of the VSG to vary dynamically with the available reactive power capacity of the energy storage system.

The overall flowchart of the proposed approach for addressing voltage violations in rural distribution networks is presented in Figure 8.

3.3. Small-Signal Stability and Modal Analysis of the Adaptive VSG Controller

To quantitatively analyze the local stability, damping characteristics, and oscillation mode behavior of the proposed adaptive VSG control strategy under different operating conditions, a small-signal model with frozen parameters is established based on the improved control architecture. Since the active-power dispatch result provided by the inner-layer optimization evolves on a slower time scale than the transient control process following a voltage disturbance, the adaptive coefficient K_{q0} calculated from (68) can be

regarded as a constant in the vicinity of any given operating point (P_{t0}, Q_{e0},E_{m0}, δ_0, ω_0) and the closed-loop system can therefore be linearized locally. At the same time, since the response speed of the virtual impedance loop and the dual inner voltage–current loops is significantly higher than that of the VSG outer loop, their fast dynamics are reflected in the small-signal characteristic analysis in the form of equivalent power sensitivity, and the influence of the adaptive Q–U loop on equivalent excitation regulation is explicitly incorporated into the closed-loop model.

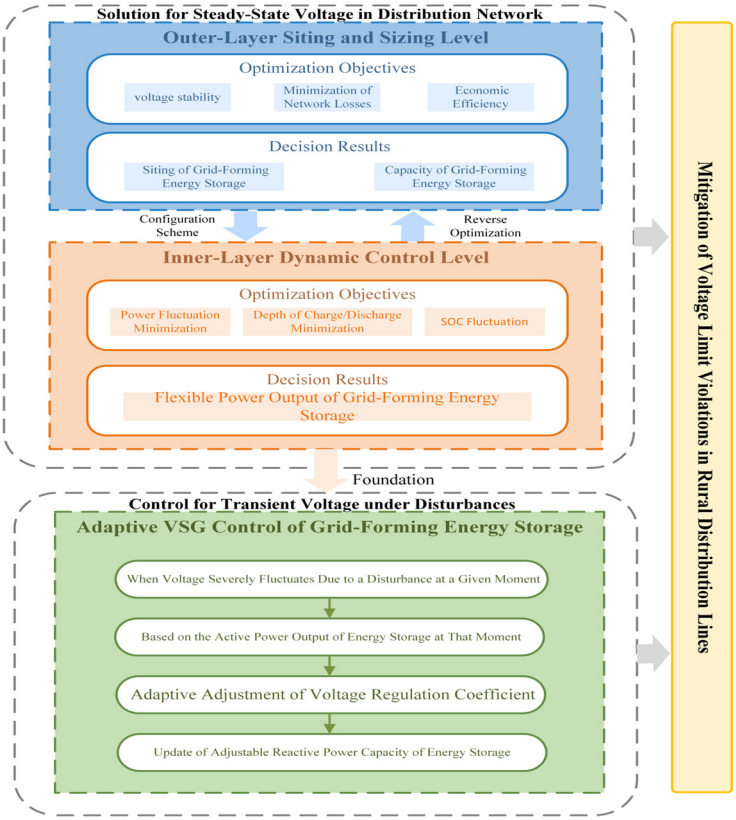


Figure 8. Overall flowchart.

3.3.1. Small-Signal Linearization of the Active Power–Frequency Loop

According to (63), define the frequency perturbation around the rated angular frequency ω_0 as $\Delta\omega = \omega - \omega_0$, and let $\Delta\delta$ denote the small perturbation of the power angle. Since the present section focuses on local stability around a given operating point, the active-power reference P_{ref} is treated as a constant.

$$\Delta P_m = K_p \Delta\omega \tag{69}$$

Accordingly, Equation (70) can be linearized as:

$$J\Delta\dot{\omega} = -\frac{1}{\omega_0}\Delta P_e - \left(D - \frac{K_p}{\omega_0}\right)\Delta\omega \tag{70}$$

From $\frac{d\delta}{dt} = \omega$ one obtains:

$$\Delta\dot{\delta} = \Delta\omega \tag{71}$$

Equations (70) and (71) describe the local dynamics of the active power–frequency loop. Under the sign convention adopted in this paper, the equivalent damping term can be written as:

$$D_{eff} = D - \frac{K_p}{\omega_0} \tag{72}$$

Equation (72) shows that the virtual inertia J and the damping coefficient D remain the key parameters determining the system's response speed, damping capability, and local stability margin.

3.3.2. Small-Signal Linearization of the Adaptive Q–U Loop

Around the operating point, the adaptive coefficient K_q is frozen at K_{q0}, and the reactive-power reference Q_{ref} is treated as a constant. For local eigenvalue analysis, the disturbance of the grid-connection voltage ΔU_n is considered as an external input and is set to zero. Therefore, Equation (64) can be linearized as:

$$\Delta E_m = -K_{q0}\Delta Q_e \tag{73}$$

Furthermore, in the vicinity of the operating point, the output active and reactive powers can be expressed in first-order form as:

$$\Delta P_e = K_{p\delta}\Delta\delta + K_{pE}\Delta E_m \tag{74}$$

$$\Delta Q_e = K_{Q\delta}\Delta\delta + K_{QE}\Delta E_m \tag{75}$$

where $K_{p\delta}$, K_{pE}, $K_{Q\delta}$ and K_{QE} denote the power sensitivity coefficients evaluated at the selected operating point. They characterize the local sensitivities of active and reactive power with respect to the power angle and the equivalent excitation voltage.

Combining (73) and (75) gives:

$$\Delta E_m = -\frac{K_{q0}K_{Q\delta}}{1 + K_{q0}K_{QE}}\Delta\delta \tag{76}$$

Substituting (76) into (74) gives:

$$\Delta P_e = \left(K_{P\delta} - \frac{K_{q0}K_{Q\delta}}{1 + K_{q0}K_{QE}}\right)\Delta\delta \equiv K_s^{eff}\Delta\delta \tag{77}$$

where K_s^{eff} is the effective synchronizing coefficient after accounting for the influence of the adaptive Q–U loop. Equation (77) shows that the adaptive coefficient does not merely reshape the time-domain response but also modifies the effective synchronizing stiffness of the closed-loop system, thereby affecting the dominant oscillatory mode.

3.3.3. Closed-Loop Characteristic Equation, Natural Frequency, and Damping Ratio

Substituting (77) into (70), together with (71), yields the second-order approximate small-signal model of the proposed adaptive VSG around the selected operating point:

$$\begin{cases} \Delta\dot{\delta} = \Delta\omega \\ J\Delta\dot{\omega} = -\left(D - \frac{K_p}{\omega_0}\right)\Delta\omega - \frac{K_s^{eff}}{\omega_0}\Delta\delta \end{cases} \tag{78}$$

Accordingly, the characteristic equation of the closed-loop system can be written as:

$$s^2 + \frac{D - \frac{K_p}{\omega_0}}{J}s + \frac{K_s^{eff}}{J\omega_0} = 0 \tag{79}$$

Based on Equation (79), the natural angular frequency, damping ratio, and damped oscillation angular frequency of the dominant mode can be expressed as:

$$\omega_n = \sqrt{\frac{K_s^{eff}}{J\omega_0}} \tag{80}$$

$$\zeta = \frac{D - \frac{K_p}{\omega_0}}{2\sqrt{JK_s^{eff}/\omega_0}} \tag{81}$$

$$\omega_d = \omega_n\sqrt{1-\zeta^2} \tag{82}$$

Based on the above equation, the root locus of the active-power loop can be plotted as shown in Figure 9.

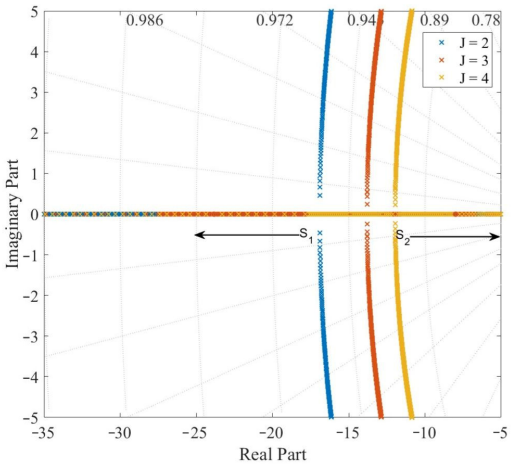


Figure 9. Root locus under different virtual inertia and damping coefficients.

As shown in Figure 9, under different virtual inertia J conditions, the dominant pole of the closed-loop system exhibits a migration pattern from a conjugate complex root to a real root as the damping coefficient D varies. When D is small, the dominant pole is located in the complex plane region of the left half-plane, and the system exhibits an underdamped state; in this case, a disturbance will be accompanied by a certain degree of oscillatory response. As D gradually increases, the pole gradually moves closer to the real axis, indicating that the system damping ratio continues to increase and the oscillation decay rate accelerates; when D increases to a certain range, the conjugate complex root eventually collapses into two real roots, and the system further transitions from an underdamped state to a state near critical damping or even overdamped. These results indicate that the damping coefficient D primarily determines the damping characteristics and damping level of the dominant mode in the active loop.

At the same time, as the virtual inertia J increases, the root locus shifts toward the imaginary axis as a whole, and the imaginary part of the dominant complex root decreases, indicating that the system's natural oscillation angular frequency decreases, and the dynamic response speed slows down accordingly. This is consistent with the pattern revealed by Equation (80): under given conditions of *K*, increasing J reduces the natural frequency of the dominant mode. Therefore, J primarily affects the system's inertial characteristics and response speed, while D primarily affects the damping level and oscillation decay capability.

4. Simulation Analysis

4.1. Establishment of the Time-Series Simulation Model

Based on historical data from the Distribution Network Cloud, D5000 system, and power consumption information collection system, the ETAP 2022 (version 22.0.1) power system simulation software is adopted. On the basis of establishing a time-series simulation model of a 10 kV distribution line in a specific region, a typical local distribution network structure, as shown in Figure 9, is extracted for time-series simulation analysis. This local network adopts a single radial structure, with the power source node as the head end, extending along the main feeder to the end, and forming branch power supplies at several nodes. The local network consists of a total of 39 nodes, with 23 equivalent loads set at distribution transformer areas. Distributed photovoltaic (DPV) sources with a capacity of 500 kW are integrated at node 8 and node 16, where DPV is installed. The loads at the distribution transformer areas are represented as total loads. Thus, the time-series simulation model of the local distribution network shown in Figure 10 is constructed for subsequent analysis of voltage and power flow characteristics under typical scenarios.

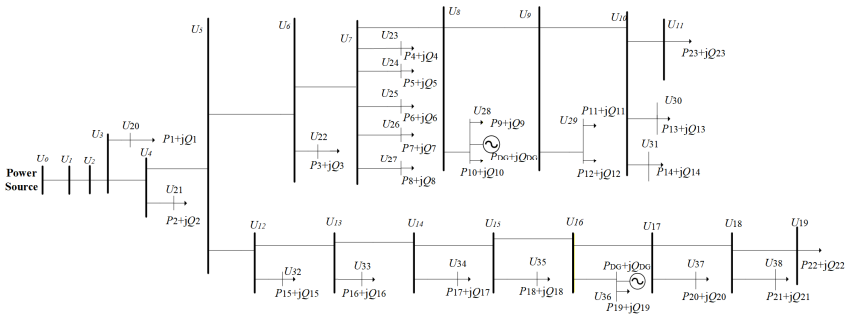


Figure 10. Topology of the local distribution network.

4.2. Typical Scenario Analysis of Distributed Photovoltaic Integration

An analysis is conducted on the distribution transformer areas where distributed photovoltaics are integrated into specific line sections. The voltage at the head-end line node, the high-side line voltage of the transformer area at node 16, and the voltage at node 36, where the low-side distributed PV is connected in the same transformer area, are selected for voltage analysis. The distribution transformer in the selected area has a capacity of 400 kVA, with 11 distributed PV users within its supply zone, a total installed capacity of 500 kW, and a PV penetration rate of 125%. Due to the different voltage levels measured, to facilitate a more intuitive comparative analysis, the voltage deviation rate (actual value/rated value) at different nodes is measured and calculated separately. The results are shown in Figure 11.

As can be observed from Figure 11, when the distributed photovoltaic output is relatively high, the voltage at PV user nodes exhibits significant variation, with pronounced voltage deviations. The PV output has a substantial impact on the grid-connection point voltage of low-voltage PV users.

Taking the actual 10 kV rural distribution network model in a certain area as the study case, the photovoltaic generation and load sample data are normalized and then classified into four typical scenarios using cluster analysis, as shown in Figure 12. Through the extraction of typical scenarios, the original fluctuating PV–load time series can be converted into multiple representative deterministic inputs, thereby avoiding excessive reliance of the analysis on a single typical day and improving both the representativeness of the model-based analysis and the applicability of the proposed method. At the same time, this approach effectively reduces the computational burden of the subsequent optimization while maintaining the required level of accuracy.

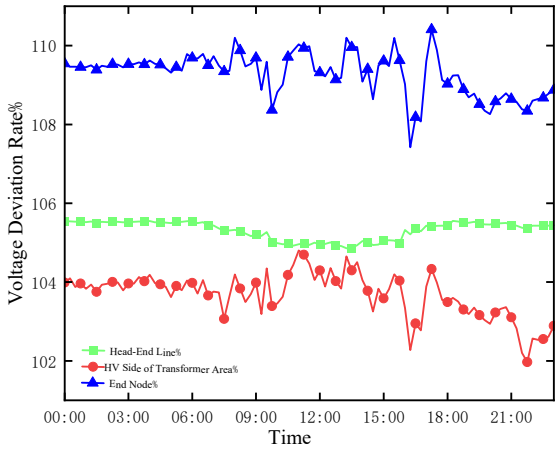


Figure 11. Voltage deviation rates at different locations after DPV integration.

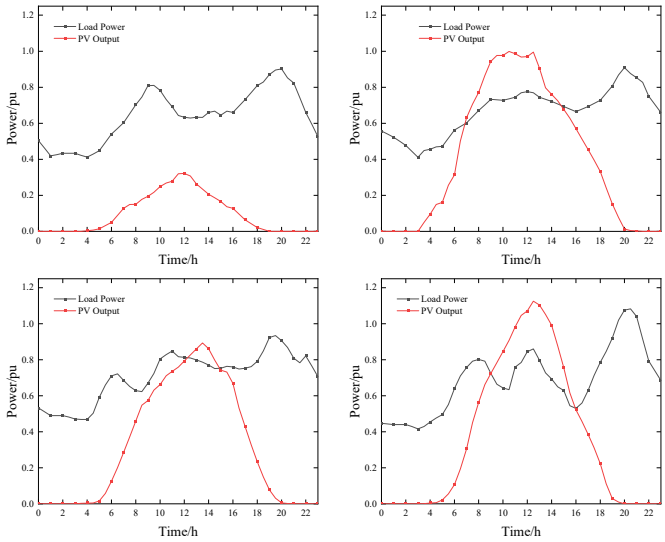


Figure 12. Typical daily distributed photovoltaic power output.

To characterize the photovoltaic integration level at the feeder scale, the PV penetration rate in this study is defined as the ratio of the total installed PV capacity in the studied feeder to the peak load of the feeder.

$$R_{PV} = \frac{P_{PV}^{inst}}{P_{load}^{peak}} \times 100\% \tag{83}$$

where P_{PV}^{inst} denotes the total installed distributed photovoltaic capacity in the studied feeder, and P_{PV}^{peak} denotes the corresponding feeder peak load.

On this basis, to investigate the effect of different PV penetration levels on node voltage distribution, PV penetration scenarios of 80%, 100%, 125%, and 140% are constructed on the same actual 10 kV feeder by proportionally scaling the total installed distributed photovoltaic capacity, while keeping the PV connection locations unchanged and the load conditions consistent. The corresponding voltage impacts under different penetration levels are shown in Figure 13.

The results indicate that, as the PV penetration level increases, the voltage rise on the low-voltage side becomes more pronounced. When the penetration level reaches 100%, the voltages at some nodes have already exceeded the allowable upper limit, indicating that the system has entered a clear high-PV-penetration operating region. For the rural distribution feeder studied in this paper, the system can be regarded as operating under

high PV penetration conditions when node voltages approach or exceed the upper limit, reverse power flow becomes more significant, and active intervention from energy storage or reactive power regulation resources is required.

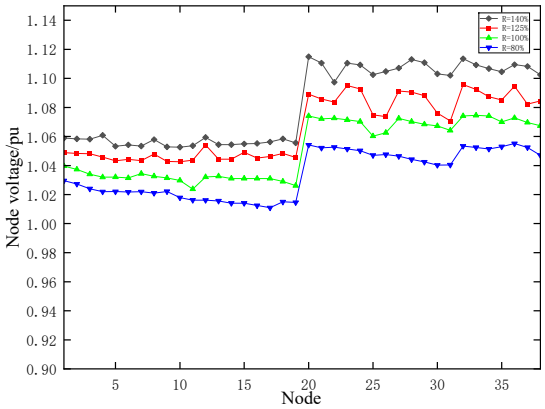


Figure 13. Voltage impacts under different PV penetration levels.

4.3. Simulation Analysis of the Dual-Layer Optimization Model

Based on the proposed dual-layer optimization model, time-series power flow calculations are carried out under three PV penetration scenarios, namely 100%, 125%, and 140%, in order to investigate the voltage over-limit issue under different penetration levels. On this basis, the outer-layer model obtains the node voltages, branch power flows, and line parameters, and further calculates the branch static voltage stability index. Meanwhile, indicators such as voltage violation risk, network loss, and voltage deviation are uniformly normalized and weighted to form a comprehensive score. After iterative optimization using the Multi-Objective Particle Swarm Optimization (MOPSO) algorithm, the optimized configuration scheme for the grid-forming energy storage system is finally determined as follows:

The comprehensive scores of each node under different PV penetration rates are shown in Figure 14.

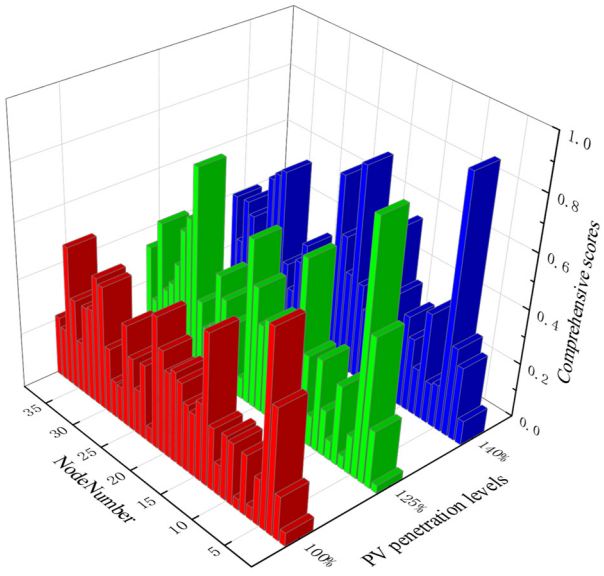


Figure 14. Comprehensive scores for each node.

Table 1 presents the specific configuration results for grid-forming energy storage systems obtained through a multi-objective optimization process using an outer-layer site selection and capacity optimization model, under different photovoltaic penetration rates.

Table 1. PV penetration rate.

PV Penetration Rate	Node	Capacity (kWh)	Power (kW)
100%	4	670.5	439.2
	13	529.7	272.7
	36	587.3	391.5
125%	4	610.2	390.2
	13	560.8	373.8
	30	569.6	378.5
140%	4	1283.1	715.5
	18	892.7	529.3
	21	1650.4	702

A comparison is conducted between the cases with and without the proposed optimization model under different PV penetration levels. The corresponding results for voltage deviation, network loss, and economic cost are presented in Table 2.

Table 2. Performance improvement of the proposed model under different PV penetration levels.

PV Penetration Rate	Voltage Deviation Improvement Rate%	Network Loss Reduction Rate%	Economic Cost Reduction Rate%
100%	14.8	15.3	29.8
125%	21.7	18.6	32.7
140%	21.4	17.8	27.8

As shown in Table 2, compared with the case without optimization, the proposed model remains effective under different PV penetration levels. The results indicate that the model can still provide both technical and economic benefits not only at the 125% PV penetration level, but also under relatively lower and higher penetration conditions considered in this study, which verifies its effectiveness and applicability across different PV penetration scenarios.

A comparative analysis of energy storage control under the MPC-based strategy and the conventional non-optimized strategy was conducted using actual measured data with the same installed capacity at a photovoltaic penetration level of 125%. The specific results are shown in Figure 15.

Based on the receding-horizon optimization control implemented in the inner-layer model, a comparative analysis is conducted between the proposed MPC-based strategy and the conventional non-optimized strategy under the same energy storage configuration. Figure 13 shows the power dispatch profiles of the grid-forming energy storage system and the corresponding SOC trajectories under the two strategies. It can be observed that the proposed MPC strategy maintains a smoother charging and discharging process during daily operation and keeps the SOC within a more coordinated operating range, demonstrating a stronger anticipatory regulation capability in response to source-load variations. In contrast, under the conventional non-optimized strategy, the energy storage system exhibits more pronounced charging and discharging fluctuations and more frequent switching between operating states, accompanied by a wider SOC variation range. This indicates that the conventional strategy lacks sufficient forward-looking coordination

during daily operation and is therefore more likely to cause power oscillations and deeper SOC fluctuations, whereas the proposed MPC strategy achieves a more balanced and orderly dispatch process.

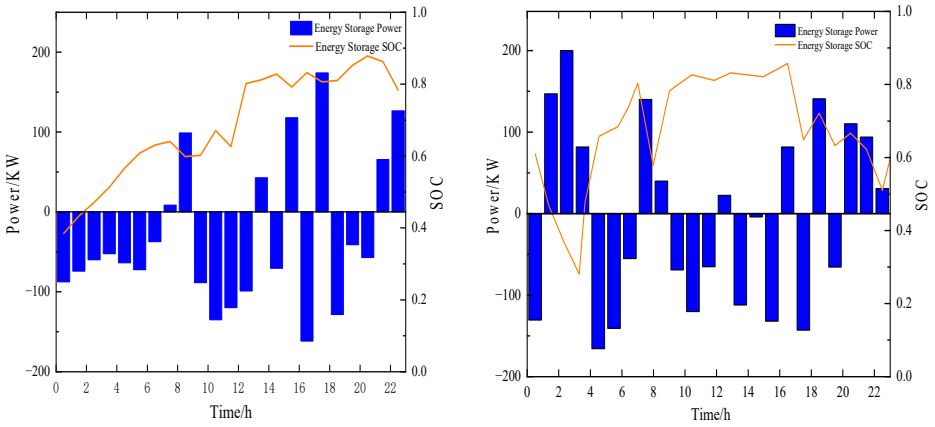


Figure 15. Comparison of different energy storage dispatch strategies: (**a**) MPC-based rolling optimization; (**b**) conventional non-optimized strategy.

To illustrate the impact of the proposed inner-layer receding-horizon optimization model on energy storage state management, the average SOC is used to reflect the maintenance level of the state of charge during daily operation, while the equivalent full cycle (EFC)count is used to characterize the cycling intensity of the battery and its potential cycle-degradation burden. Therefore, this study selects the average SOC and the equivalent full cycle count as two indicators of energy storage operating stress to compare the proposed MPC strategy with the conventional non-optimized strategy.

As shown in Table 3, compared with the conventional non-optimized strategy, the proposed MPC strategy exhibits superior operating characteristics in terms of both the average SOC and the equivalent full cycle count. While maintaining a relatively stable state-of-charge level, the MPC strategy reduces the equivalent full cycle count of the energy storage system, indicating that it can reduce unnecessary charge–discharge repetitions while satisfying operational regulation requirements, thereby alleviating the cycling burden on the battery. In contrast, under the conventional non-optimized strategy, the energy storage system is more likely to undergo frequent switching between charging and discharging states and larger SOC fluctuations, which lead to higher cycling intensity and further aggravate the long-term cycle degradation trend of the battery. Furthermore, the optimized coordination of the charging and discharging process under the proposed MPC strategy also improves the feeder-level power distribution characteristics. The feeder power results under the MPC strategy are shown in Figure 16.

Table 3. Comparison of average SOC and equivalent full cycles under different strategies.

Strategy	Average SOC	EFC
Conventional non-optimized strategy	0.651	1.32
Proposed MPC strategy	0.695	1.12

It can be observed from Figure 16 that, without the integration of the energy storage system, the power at the substation outgoing line decreases significantly during periods of high PV output, with reverse power flow occurring around midday, indicating that the distributed PV output exceeds the local load demand. In contrast, after the integration of the

grid-forming energy storage system, the magnitude of reverse power flow is substantially reduced. During nighttime and peak load periods, the energy storage system participates in power supply, resulting in a lower output power at the substation outgoing line compared to the scenario without energy storage. The results demonstrate that the integration of the grid-forming energy storage system can effectively absorb surplus distributed PV energy and participate in load supply, thereby mitigating reverse power flow during typical daily operation and improving the power flow distribution characteristics of the distribution network.

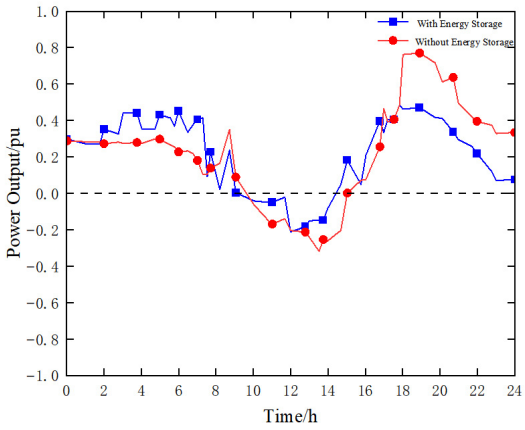


Figure 16. Comparison of feeder power with and without energy storage.

In the proposed bi-level optimization model, the outer layer employs a Multi-Objective Particle Swarm Optimization algorithm to optimize the siting and sizing of grid-forming energy storage systems, and its convergence process is illustrated in Figure 17. As can be observed from Figure 17, the adopted optimization algorithm converges rapidly in the early iterations and gradually stabilizes in the later stage, indicating that it possesses good convergence performance and is capable of obtaining stable optimization results.

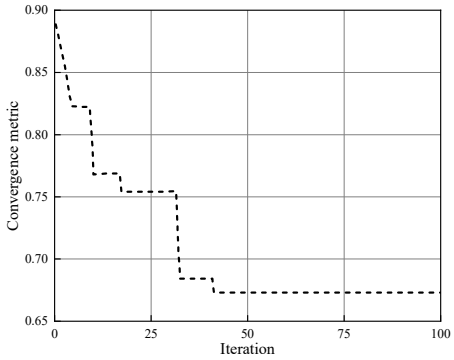


Figure 17. Convergence process of the optimization algorithm.

4.4. Analysis of the Effect of Adaptive VSG on Voltage Support Performance

4.4.1. Analysis of Voltage Support Effect Under Load Disturbances

To verify the transient voltage support capability of the proposed adaptive VSG control strategy under disturbance conditions, based on the aforementioned siting and sizing optimization results of the grid-forming energy storage system, node 13 is selected from the configured grid-forming energy storage integration nodes as the study object, and a corresponding transient simulation model is established. Using the parameters listed in Table 4, a comparative analysis of the transient response characteristics of node voltage and reactive power under different VSG control strategies is conducted.

Table 4. Basic system parameters.

Parameter	Value
DC bus voltage/V	1000
Grid voltage/V	380
System frequency/Hz	50
Filter inductor L_f/mH	5
Filter capacitor C_f/μF	35
Initial virtual inertia J	3
Damping coefficient D	100

In the simulation system, a voltage step disturbance is introduced at t = 2.0t = 2.0t = 2.0 s. Specifically, the grid voltage is reduced to 0.75 pu and then restored to 1.0 pu at t = 3.0t = 3.0t = 3.0 s. The voltage waveforms at the grid connection point under different control strategies are shown in Figure 18.

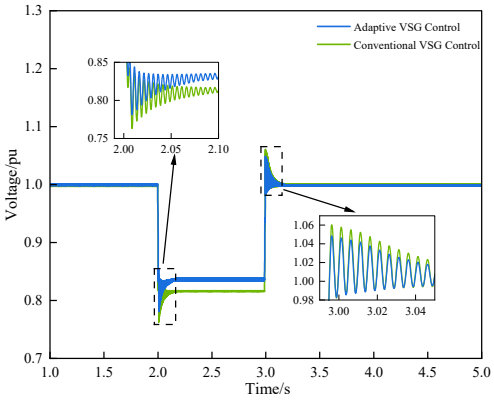


Figure 18. Voltage waveforms at the grid connection point under different control strategies.

As can be observed from Figure 18, at the moment the disturbance occurs, the voltage at the grid connection point under both control strategies exhibits a transient drop; however, a difference lies in the magnitude of this transient drop. With conventional VSG control, the grid connection point voltage drops to 0.81 pu. In contrast, with adaptive VSG control, the voltage drops to 0.83 pu. The results demonstrate that the adaptive VSG control strategy can effectively mitigate the transient voltage drop magnitude at the grid connection point.

As can be observed from Figure 19, following the occurrence of the disturbance, the grid-forming energy storage system under both control strategies is capable of responding rapidly and outputting reactive power to participate in voltage regulation. However, there is a notable difference in the magnitude of the reactive power output between the two control strategies. With conventional VSG control, the magnitude of the reactive power output is relatively small. In contrast, under adaptive VSG control, the energy storage system is able to deliver a larger amount of reactive power, with the response magnitude being significantly higher than that of conventional VSG control under both charging and discharging conditions.

4.4.2. Analysis of the Impact of Reactive Power Capacity Limits on Voltage Support Performance

Considering that the voltage support capability of a grid-forming converter depends not only on the control strategy itself but also on its available reactive power capacity, under severe disturbances, as the demand for reactive power support continues to increase, the converter output may gradually approach its capacity limit, thereby affecting its actual voltage support performance. Therefore, to further evaluate the operating characteristics

of the proposed adaptive control strategy under reactive power capacity constraints, the maximum reactive power capacity limit is set to 0.7 pu, and simulations are carried out for the system operating under the proposed adaptive control strategy in response to both a load disturbance and a three-phase ground fault.

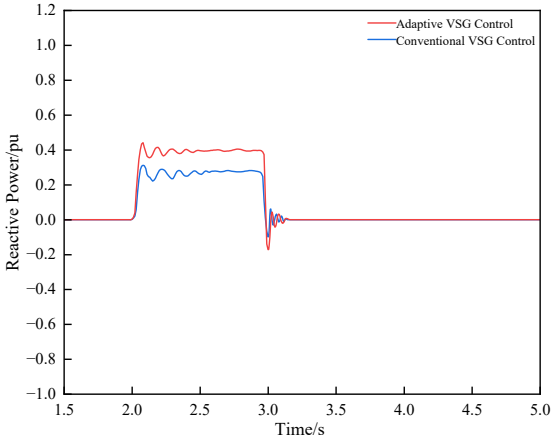


Figure 19. Reactive power waveforms under different control strategies.

In the simulation system, a voltage step disturbance is introduced at t = 2.0 s. Specifically, the grid voltage is reduced to 0.75 pu and then restored to 1.0 pu at t = 3.0 s. The corresponding reactive power waveforms of the energy storage system are shown in Figure 18, and the simulated grid-connected terminal voltage responses with and without imposing a maximum reactive power limit of 0.7 pu are shown in Figure 19.

As shown in Figure 20, since the reactive power provided by the energy storage system during the voltage step disturbance does not exceed the prescribed limit of 0.7 pu before the maximum reactive power limit is imposed, the influence of the added reactive power limit on system operation is not significant. Therefore, as shown in Figure 21, the grid-connected terminal voltage responses of the energy storage system before and after imposing the reactive power limit are generally similar.

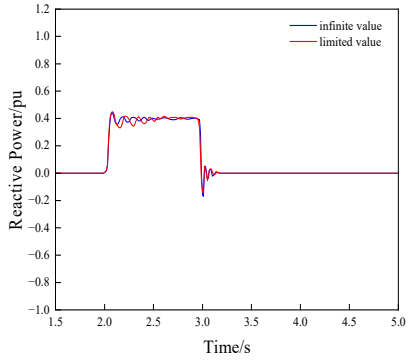


Figure 20. Reactive power waveforms under voltage step disturbance with and without reactive power limit.

A three-phase short-circuit fault is applied at the midpoint of the transmission line at t = 2 s and cleared 0.5 s later. The reactive power waveforms of the energy storage system before and after imposing a maximum reactive power limit of 0.7 pu are shown in Figure 22, and the corresponding grid-connected terminal voltage responses are shown in Figure 23.

As shown in Figure 22, during the three-phase short-circuit fault, the reactive power output of the energy storage system is significantly constrained after imposing the maximum reactive power limit, and its reactive power support capability is lower than that in

the unlimited case. Therefore, as shown in Figure 23, after imposing the reactive power limit, the reactive power provided by the energy storage system for transient voltage support is reduced, thereby weakening the voltage recovery effect.

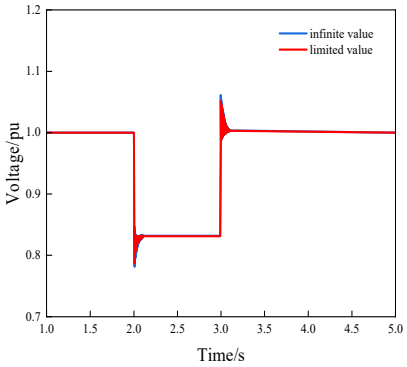


Figure 21. Terminal voltage responses under voltage step disturbance with and without reactive power limit.

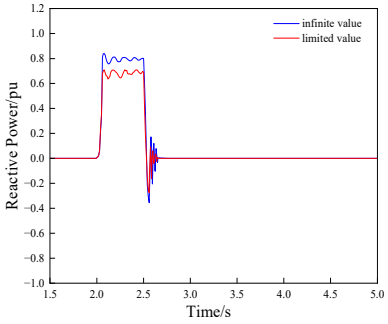


Figure 22. Reactive power waveforms under three-phase short-circuit fault with and without reactive power limit.

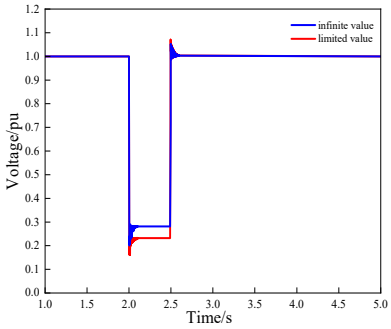


Figure 23. Reactive power waveforms under three-phase short-circuit fault with and without reactive power limit.

5. Conclusions

Focusing on the challenges of voltage over-limit issues in distribution networks under high-penetration distributed photovoltaic (DPV) integration in rural areas, as well as the insufficient voltage support capability under disturbance conditions, this paper proposes a dual-layer optimized configuration and adaptive VSG control method for grid-forming energy storage systems aimed at coordinated steady-state and transient voltage regulation. Through systematic research encompassing mechanism analysis, model construction, and simulation verification, the following conclusions are drawn:

By comprehensively considering multiple factors such as static voltage stability and voltage deviation, the optimized configuration scheme of grid-forming energy storage can

not only effectively mitigate overvoltage on the low-voltage user side, alleviate reverse power flow during operation, and enhance the safety and stability of distribution network operation, but also help improve the coordinated regulation capability of energy storage during intraday operation, promote a better match between charging/discharging behavior and state-of-charge management, and balance voltage mitigation performance with the long-term operation of the equipment.

The adaptive reactive power–voltage droop control strategy proposed within the VSG control framework dynamically adjusts the reactive power regulation capability according to the active power output state of the grid-forming energy storage. Transient simulation results demonstrate that, compared with conventional fixed-parameter VSG control, the proposed strategy exhibits superior voltage support capability under disturbance conditions, reduces the magnitude of voltage oscillations, and fully utilizes the reactive power support potential of the energy storage system. At the same time, the results under reactive power capacity constraints show that the voltage support improvement is achieved within the converter capability boundary. When the reactive power limit is not reached, its influence is negligible, whereas under severe faults the reactive power constraint weakens the voltage recovery effect.

Future work will further extend the proposed model to more complex and even meshed distribution network structures in order to evaluate its adaptability under stronger network coupling and more diverse operating conditions. In addition, future studies will take into account operator-initiated curtailment actions and incorporate the influence of dynamic electricity pricing in energy markets on distributed photovoltaic systems into the model analysis, thereby developing a more practically valuable research framework that simultaneously considers network security, control performance, and market mechanisms.

Author Contributions: Conceptualization, investigation and data curation, Y.T., H.L. and S.C.; writing—original draft, T.W.; writing—review and editing, T.W. and H.C.; project administration, H.C. All authors have read and agreed to the published version of the manuscript.

Funding: This research was supported by the Doctoral Scientific Research Start-up Foundation Program of Department of Science and Technology of Liaoning Province, grant number 2024-BSLH-271.

Data Availability Statement: The data supporting this study can be obtained from the corresponding author upon request. They are not publicly accessible due to privacy considerations.

Conflicts of Interest: Author Ye Tian was employed by the Electric Power Research Institute of State Grid Liaoning Electric Power Co., Ltd. Authors Hui Li and Shang Chen were employed by the China Electric Power Research Institute Wuhan Branch. The remaining authors declare that the research was conducted in the absence of any commercial or financial relationships that could be construed as a potential conflict of interest.

Abbreviations

The following abbreviations are used in this manuscript:

DPV	Distributed Photovoltaic
ESS	Energy Storage System
SOC	State of Charge
VSG	Virtual Synchronous Generator
MOPSO	Multi-Objective Particle Swarm Optimization
MPC	Model Predictive Control
TOPSIS	Technique for Order Preference by Similarity to Ideal Solution
ETAP	Electrical Transient Analyzer Program

EFC	Equivalent Full Cycle
PV	Photovoltaic
DC	Direct Current

Appendix A

Appendix A.1

This appendix examines a typical 39-node local distribution network structure consistent with the examples in the main text. It evaluates the accuracy of static voltage stability indicators and the impact of neglecting branch parallel admittance, and provides corresponding supplementary numerical results.

Table A1. Statistics on Global Errors in Circuit Models with and without Parallel Admittance.

Metric	Title 2
Maximum absolute error	4.6380×10^{-5}
Mean absolute error	2.5776×10^{-6}
Maximum relative error (%)	0.025216
Mean relative error (%)	0.003787

Table A2. Identification Results of the Top 10 Weak Branches With and Without Considering Line Shunt Admittance.

Rank	Without Shunt Admittance	With Shunt Admittance
1	4–21	4–21
2	3–20	3–20
3	10–30	10–30
4	7–27	7–27
5	7–28	7–28
6	13–33	13–33
7	9–29	9–29
8	10–31	10–31
9	7–25	7–25
10	7–24	7–24

Appendix A.2

To clarify the effect of impedance characteristics on the approximation error introduced by neglecting branch shunt admittance, controlled parameter scans are performed on the same 39-node typical local distribution network structure used in the main text. Two cases are considered. In the first case, the impedance magnitude $|Z_{ij}|$ was scaled while the original R/X ratio of each branch was kept unchanged. In the second case, the R/X ratio was scaled while the impedance magnitude $|Z_{ij}|$ was kept unchanged. The resulting mean and maximum relative errors of the voltage stability index are summarized in Tables A3 and A4.

Table A3. Effect of impedance magnitude with fixed R/X.

Scaling Factor of $\|Z\|$	Mean Relative Error (%)	Maximum Relative Error (%)
0.25	0.0009279	0.0062784
0.5	0.0018684	0.012574
1	0.003787	0.025216
2	0.0077726	0.050706
4	0.016322	0.1025

Table A4. Effect of R/X with fixed impedance magnitude.

Scaling Factor of R/X	Mean Relative Error (%)	Maximum Relative Error (%)
0.25	0.0056718	0.034077
0.5	0.0046452	0.029532
1	0.003787	0.025216
2	0.0043096	0.02322
4	0.0032397	0.0237

Tables A3 and A4 show that the approximation error increases mainly with impedance magnitude, whereas the effect of R/X variation is limited. For the feedline considered in this study, the resulting error remains low.

References

1. Cai, M.; Wu, Z.; Xia, Y.; Lai, X.; Li, Y. Mechanism analysis and mitigation methods for voltage limit violations in distributed PV transformer areas. *Jiangxi Electr. Power* **2025**, *49*, 7–12.
2. Diahovchenko, I.; Morva, G.; Chuprun, A.; Keane, A. Comparison of voltage rise mitigation strategies for distribution networks with high photovoltaic penetration. *Renew. Sustain. Energy Rev.* **2025**, *212*, 115399. [CrossRef]
3. Liu, J.; Qiu, Z.; Zhang, Z.; Zhu, C.; Zhang, X. Research on distributed photovoltaic integration strategies for rural distribution networks. *Rural Electrif.* **2025**, *11*, 40–43+87. [CrossRef]
4. Liu, A.; Li, X.; Li, Y.; Hao, S.; Miao, Y.; Zheng, Y.; Xie, J.; Yao, Q. Collaborative scheduling method of active-reactive power for rural distribution systems with a high proportion of renewable energy. *Front. Energy Res.* **2024**, *12*, 1410694. [CrossRef]
5. Hu, C.; Chen, H.; Tang, A. Sliding mode control strategy of grid-forming energy storage converter with fast active support of frequency and voltage. *Front. Energy Res.* **2024**, *12*, 1416591. [CrossRef]
6. Yin, K.; Xiao, Y.; Shen, X.; Zhu, Y.; Yang, Y. Review of photovoltaic–battery energy storage systems for grid-forming operation. *Batteries* **2024**, *10*, 288. [CrossRef]
7. Ruan, P.; Su, Q.; Zhang, L.; Luo, J.; Diao, Y.; Xie, L.; Zheng, H. Optimal siting and sizing of hybrid energy storage systems in high-penetration renewable energy systems. *Energies* **2025**, *18*, 2196. [CrossRef]
8. Xiong, W. Static voltage stability analysis of distribution networks with high-proportion distributed generation integration. *Jiangxi Electr. Power* **2024**, *48*, 11–15.
9. Xiao, Y.; Xiao, X.; Jin, X.; He, X.; Feng, J.; He, X. Multi-objective optimization of distribution network systems with energy storage and distributed PV considering static voltage stability. *Guangdong Electr. Power* **2024**, *37*, 24–32.
10. Zhang, K.; Zhang, G.; Xu, B.; Cui, X.; Zhang, X.; Mu, C. Optimized capacity configuration method for energy storage considering voltage risk in distribution networks with high-proportion renewable energy. *Insul. Surge Arresters* **2023**, *6*, 85–93. [CrossRef]
11. Wu, Z.; Wang, L.; Li, M.; Wang, B.; Liu, X.; Zhang, B.; Ma, Z. Research on long-term process simulation of distribution networks with high-penetration distributed photovoltaic. *J. Phys. Conf. Ser.* **2026**, *3192*, 012034. [CrossRef]
12. Mou, X.; Chen, W.; Li, X. Refined Fuzzy-Control-Based VSG Control Strategy for Flexible Interconnection Devices in Distribution Grid. *Electronics* **2025**, *14*, 4310. [CrossRef]
13. Pan, M.; Tan, Y.; Liu, H.; Bai, H.; Huang, G.; Liu, Y. A VSG transient improvement method from the perspective of equivalent circuits. *Energies* **2026**, *19*, 1575. [CrossRef]
14. Zhang, Y.; Zhou, S.; Zhang, L.; Lu, X.; Li, B. VSG frequency control strategy for grid-connected inverters based on fuzzy rule and weight-adaptive MPC. *Proc. CSU-EPSA* **2025**, *in press*. Available online: https://link.cnki.net/urlid/12.1251.tm.20251216.1753.005 (accessed on 8 April 2026).
15. Zhang, H.; Pan, H.; Chen, Y.; Luo, C.; Xu, J.; Tan, W. Adaptive transient stability control strategy for VSG considering frequency dynamic response. *Power Syst. Prot. Control* **2025**, *53*, 90–100. [CrossRef]
16. Wu, M.; Lyu, Z.; Song, Z.; Lv, Z.; Xiong, X. Distributed secondary reactive power-voltage control strategy for independent virtual synchronous microgrid. *Electr. Power Autom. Equip.* **2022**, *42*, 63–71. [CrossRef]
17. Sun, J.; Li, F.; Chen, J.; Fu, B.; Gao, Q. Voltage and reactive power coordinated control system for grid-forming energy storage and VSG control based on intelligent algorithm. *Electron. Des. Eng.* **2025**, *33*, 20–24. [CrossRef]
18. An, K.; Gao, Y. Research on voltage control strategy for distributed PV grid-connected inverters. *Technol. Mark.* **2024**, *31*, 65–68.
19. Valdez, J.; Carrión, D. Hybrid transmission schemes for enhancing static voltage stability in power systems under variable operating conditions. *Energies* **2026**, *19*, 3. [CrossRef]
20. Zhang, Q.; Liao, Q.; Tang, F.; Xu, J.; Liu, S.; Zou, H. Static voltage stability assessment method for distribution networks considering distributed generation integration. *Autom. Electr. Power Syst.* **2015**, *39*, 42–48. [CrossRef]

21. Gu, S.; Lu, Y.; Gu, H. Comparative study on static voltage stability indices of new energy power station grid-connected system. *J. Eng. Res. Rep.* **2025**, *27*, 524–532. [CrossRef]
22. Liu, S.; Liu, H.; Zhang, J.; Yu, S.; Sun, D.; Xing, J.; Gao, B. Analysis of factors influencing VSG voltage support and improved control strategy based on equivalent impedance. *Trans. China Electrotech. Soc.* **2025**, *40*, 2738–2751. [CrossRef]

Disclaimer/Publisher's Note: The statements, opinions and data contained in all publications are solely those of the individual author(s) and contributor(s) and not of MDPI and/or the editor(s). MDPI and/or the editor(s) disclaim responsibility for any injury to people or property resulting from any ideas, methods, instructions or products referred to in the content.